Materials Today Physics 37 (2023) 101211

Contents lists available at ScienceDirect

Materials Today Physics

journal homepage: www.journals.elsevier.com/materials-today-physics

Entropy-driven structural transition from Tetragonal to Cubic phase: High Thermoelectric Performance of $CuCdInSe_3$ compound

Tingting Luo [a,1], Yihao Hu [b,c,1], Shi Liu [c], Fanjie Xia [a], Junhao Qiu [a], Haoyang Peng [a], Keke Liu [a], Quansheng Guo [d], XingZhong Li [e], Dongwang Yang [a], Xianli Su [a,**], Jinsong Wu [a,***], Xinfeng Tang [a,*]

[a] State Key Laboratory of Advanced Technology for Materials Synthesis and Processing, Wuhan University of Technology, Wuhan, Hubei, 430070, China
[b] Zhejiang University, Hangzhou, Zhejiang, 310058, China
[c] Key Laboratory for Quantum Materials of Zhejiang Province, Department of Physics, School of Science, Westlake University, Hangzhou, Zhejiang, 310024, China
[d] School of Materials Science and Engineering, Hubei University, Wuhan, Hubei, 430062, China
[e] Nebraska Center for Materials and Nanoscience, University of Nebraska, Lincoln, NE, 68588, USA

ARTICLE INFO

Keywords:
$CuCdInSe_3$
Cubic zinc blende
DFT+U
Thermoelectric performance
Cd doping

ABSTRACT

Cu based chalcopyrite is an important class of thermoelectric materials with excellent electronic properties, however, the thermal conductivity is relatively high due to the simple tetragonal structure with highly ordered configuration on cation sites, limiting the thermoelectric performance. Herein, we realize that the modulation of entropy via alloying CdSe achieves the structural transition from tetragonal structure with ordered configuration on cations sites in $CuInSe_2$ compound to cubic $CuCdInSe_3$. $CuCdInSe_3$ crystallizes in a zinc blende (ZnS) structure where Cu, Cd and In cations randomly occupy the Zn site with the occupancy fraction 1/3. This entropy driven order-disorder transition on the cation site, in conjunction with the intensified point defect phonon scattering via alloying CdSe in $CuInSe_2$, dramatically suppress the thermal conductivity. An ultra-low thermal conductivity of 0.76 $Wm^{-1}K^{-1}$ at 780 K is achieved for $CuCdInSe_3$ compound, which is only about 2/3 in comparison with that of $CuInSe_2$. $CuCdInSe_3$ is an indirect semiconductor, with the minimum of conduction band (CBM) located at Γ point and the maximum of valence band (VBM) between Γ and A. The density of states in VBM of $CuCdInSe_3$ are mainly contributed by the hybridization between Se-4p and Cu-3d orbitals, while that of CBM is dominant by Se-4p and In-5s orbitals. Minute adjustment of Cd content in $CuCd_{(1+x)}InSe_3$ effectively modulates the carrier concentration and an optimized power factor of 0.58 $Wm^{-1}K^{-2}$ is attained at 578 K for $CuCd_{1.01}InSe_3$, which is 9.6 times as high as the pristine $CuCdInSe_3$. The improved electronic properties integrated with the intrinsically low thermal conductivity result in an enhanced thermoelectric figure-of-merit *ZT* value of 0.45 at 780 K for $CuCd_{1.005}InSe_3$, which is seven times higher than that of the pristine $CuCdInSe_3$.

1. Introduction

Thermoelectric (TE) materials are a type of functional material capable of directly converting heat into electricity through the transportation of charge carriers and phonons within solid materials. Thermoelectric technology has garnered significant attention due to its immense potential to provide a safe, reliable, and all-solid strategy for power generation and refrigeration [1–3]. The performance of TE materials is usually evaluated by the dimensionless figure of merit $ZT = \sigma S^2 T/(\kappa_e + \kappa_L)$, where σ is the electrical conductivity, S is the Seebeck coefficient, T is the absolute temperature, κ_e is the electronic thermal conductivity, and κ_L is the lattice thermal conductivity, respectively [4,5]. Thermoelectric materials with high performance require low thermal conductivity and excellent electrical transport properties (normally a high power factor $PF = \sigma S^2$). However, these three physical parameters of electrical conductivity, Seebeck coefficient and total thermal

* Corresponding author.
** Corresponding author.
*** Corresponding author.
E-mail addresses: suxianli@whut.edu.cn (X. Su), wujs@whut.edu.cn (J. Wu), tangxf@whut.edu.cn (X. Tang).
[1] Tingting Luo and Yihao Hu contributed equally to this paper.

https://doi.org/10.1016/j.mtphys.2023.101211
Received 22 July 2023; Received in revised form 18 August 2023; Accepted 22 August 2023
Available online 22 August 2023

conductivity ($\kappa_e + \kappa_L$) are interrelated, so it is difficult to improve *ZT* by only regulating one parameter. In recent years, tremendous investigations demonstrate that the thermoelectric properties can be improved by a synergistic modulation of these parameters via the strategies including electronic band engineering [6–9], forming solid solution [10–12], nanostructuring [13–15], defect engineering [16–18] and entropy engineering [19–21], *etc*.

Entropy engineering has been applied in numerous research by transforming low symmetry TE materials into a high symmetric cubic structure, such as GeTe/MnTe [11], $AgBiSe_2$/PbSe [21], $(SnSe)_{0.5}(AgSbSe_2)_{0.5}$ [22], $PbGeSnCd_xTe_{3+x}$ [23], *etc*. The entropy-driven structural transformations from lower to higher symmetric crystal structures have a significant effect on thermal transport and thermoelectric properties. The increasing entropy via forming solid solution with muti-components enhances defect phonon scattering, thus sharply suppressing the thermal conductivity. It is noted that among these high-performance thermoelectric materials, most of the compounds possess cubic or highly symmetric crystal structures with low thermal conductivity. Therefore, it is of great importance to explore TE materials with highly symmetric structures and intrinsically low lattice thermal conductivity, of which the extraordinary thermoelectric performance is expected.

Recently, I-III-VI_2 (I═Cu,Ag; III═Ga,In; VI═S,Se,Te; Space group $I\bar{4}2d$) chalcopyrite with the diamond-like structure have attracted lots of interests in the field of thermoelectric due to their highly tunable crystal structures and electronic band structures, leading to highly tunable physical properties [24,25]. Chalcopyrite compounds composed of various elements have a crystal structure similar to cubic zinc blende, which generally possess a tetragonal (non-cubic) structure with distorted tetrahedra, and they have a doubled unit cell in the z-direction due to the ordered arrangement on different types of cations [26]. Moreover, the anionic sublattice presents a locally distorted non-cubic framework. Noted that the non-cubic structure and the order configuration on the cation sites result in the energy splitting in the top of valence band and the bottom of conduction band, which is unfavorable to the thermoelectric properties [26,27]. In addition, the ordered configuration on the cation sites lead to the high thermal conductivity especially for Cu based chalcopyrite, severely hindering the improvement of their thermoelectric properties. Therefore, the disordered configuration on the cation sites is highly desirable for Cu-based chalcopyrite.

In this study, an entropy driven structural phase transition from tetragonal structure with ordered configuration on cations sites in $CuInSe_2$ compound to cubic structured $CuCdInSe_3$ (zinc blende structure, space group $F\bar{4}3m$) is realized via alloying CdSe. We systematically investigated the crystal structure, electronic band structure and thermoelectric properties of $CuCdInSe_3$. The stochastically disordered cations of $CuCdInSe_3$ lead to strong alloying scattering, which can efficiently scatter thermal phonons, resulting in a low lattice thermal conductivity. Meanwhile, the electronic band structure of the $CuCdInSe_3$ compound was studied by the pseudo-hybrid Hubbard density functional, Agapito-Curtarolo-Buongiorno Nardelli (ACBN0) method. In addition, $CuCd_{(1+x)}InSe_3$ (x = 0.25%, 0.5%, 1%, 2%) with excess Cd doping exhibit n-type conduction at 300–780 K. It is found that the carrier concentration of $CuCdInSe_3$ compounds can be considerably enhanced by tiny Cd doping. At the same time, high mobility and Seebeck coefficient have been maintained, and the lattice thermal conductivity is reduced by Cd doping, which promotes the peak *ZT* value to 0.45 at 780 K for $CuCd_{(1+x)}InSe_3$ (x = 0.5%).

2. Experimental section

2.1. Synthesis

High purity Cu (ingot , 99.999%), Cd (shots , 99.999%), In (pellet , 99.999%) and Se (shots , 99.999%) were weighed according to the corresponding stoichiometric ratio of CdSe, $CuInSe_2$ and $CuCd_{(1+x)}InSe_3$ (x = 0, 0.25%, 0.5%, 1%, 2%), respectively. The ingots of the above samples were prepared by vacuum melting at 1373 K for 24 h, which were separately ground into fine powders and loaded into a graphite mold with an inner diameter of 16 mm. Then, a dense disk sample was prepared by a spark plasma vacuum-sintering (Ed-PAS-III, Elenix, Japan) under a pressure of 40 MPa at 953 K for 10 min. The relative density (ρ) of all sintered pellets is above 97%, indicating all pellets are dense.

2.2. Characterization

The phase composition of the samples were verified by powder X-ray diffraction (XRD, PANalytical, Cu Kα) at an operating voltage of 40 kV and a current of 40 mA. The XRD pattern was refined by Rietveld using FullProf software. The back-scattered electron images (BSEI) and corresponding Energy Dispersive X-ray Spectrometer (EDS) maps of sintered bulk samples were performed by electron probe microscopy (EPMA, JXA 8230, JEOL). The surface element and valence states of the bulk samples were detected by X-ray photoelectron spectroscopy (XPS, VG Multilab 2000). The optical band gap of the sample was measured by a spectrophotometer (Lambda 750 S). The thermal stability of the sample was characterized by differential scanning calorimetry (DSC, TA, Q20) in a nitrogen atmosphere with a temperature range from room temperature to 1073 K at a heating rate of 10 K/min. The bulk sample was processed into a thin slice by the focused ion beam milling (FIB, Helios NanoLab G3 UC, FEI). TEM/STEM characterizations were performed on a double C_S-corrected transmission electron microscope (Titan Themis G2 60–300, FEI). The sound velocity of the sample at room temperature was measured by an integrated sound velocity measurement system (consisting of ultrasonic pulse receiver Panametrics 5072 PR and oscilloscope TDS 2022).

2.3. Transport property measurements

The electrical conductivity (σ) and the Seebeck coefficient (*S*) were measured simultaneously by a commercial equipment (ZEM-3, Ulvac Riko, Japan) under a helium atmosphere from 300 K to 780 K. The thermal conductivity (κ) was calculated by $\kappa = D\rho C_p$, where *D* is the thermal diffusivity and measured in an argon atmosphere by the laser flash diffusivity method (LFA 457, Netzsch, Germany), the heat capacity (C_p) was estimated by the Dulong−Petit law, and the sample density (ρ) was determined by Archimedes method. The electrical conductivity (σ) and the Hall coefficient (R_H) at low temperatures from 10 K to 300 K were measured by a Physical Property Measurement System (PPMS-9T, Quantum Design, USA). The corresponding carrier concentration (*n*) and the carrier mobility (μ) were calculated from $n = 1/e|R_H|$ and $\mu = \sigma/ne$ based on a single parabolic band model. In addition, the heat capacity at low temperatures from 4 K to 300 K was obtained by the PPMS-9T.

3. Results and discussion

3.1. Crystal structure and microstructure analysis

Powder X-ray diffraction (XRD) patterns of the as-synthesized CdSe, $CuInSe_2$ and $CuCdInSe_3$ are presented in Fig. 1(a), which indicates that the samples are crystallized well. All of the diffraction peaks for CdSe can be indexed to the hexagonal wurtzite structure with a space group of $P6_3/mc$ (ICSD PDF #08–0459), and the XRD pattern of $CuInSe_2$ can be indexed as chalcopyrite structure with the space group of $I\bar{4}2d$ (ICSD PDF #40–1487). Rietveld refinement (Fig. 1(b)) [28] on the XRD pattern of $CuCdInSe_3$ yielded a cubic zinc blende structure (Fig. 1(c)) [29] with a cell parameter $a = b = c = 5.889$ Å, $\alpha = \beta = \gamma = 90°$, bigger than that of $CuInSe_2$ ($a = b = 5.782$ Å) owing to the larger atomic radius

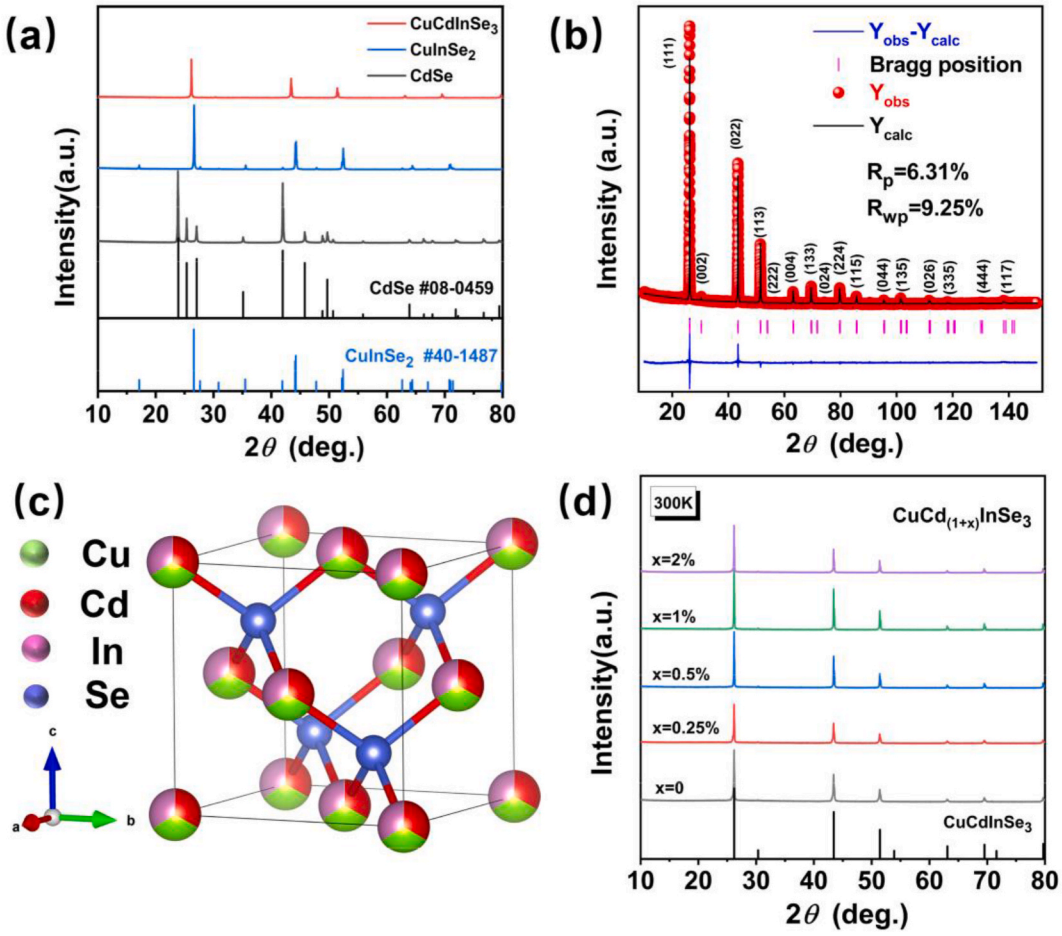

Fig. 1. (a) Powder X-ray diffraction (XRD) patterns of CdSe, $CuInSe_2$ and $CuCdInSe_3$. The CdSe #08–0459 belongs to a wurtzite phase with the space group of $P6_3/mc$, $a = b = 4.299$Å, $c = 7.010$ Å, $V = 112.2$ Å ^{3}. The $CuInSe_2$ #40–1487 crystallizes in the space group of $I\bar{4}2d$ with $a = b = 5.782$ Å, $c = 11.619$ Å, $V = 388.4$ Å ^{3}. (b) Rietveld refinement of the powder XRD pattern of $CuCdInSe_3$. (c) Zinc blende structure of $CuCdInSe_3$. (d) Powder X-ray diffraction (XRD) patterns of $CuCd_{(1+x)}InSe_3$ (x = 0, 0.25%, 0.5%, 1%, 2%).

of Cd (1.57 Å) than Cu (1.28 Å). In addition, the Cu, Cd and In cations are considered to be statistically disordered at the coordinate of (0, 0, 0) in this cubic structure, as shown in Fig. 1(c). This indicates that the tetragonal structure of $CuInSe_2$ can be destabilized and converted to a cubic structure, presumably by the entropy-driven alloying of the equimolar fraction of CdSe to form the cubic phase of $CuCdInSe_3$. With the increase of elemental species, the configurational entropy is boosted and the symmetry of the crystal structure may be improved [30]. XRD patterns of the sintered $CuCd_{(1+x)}InSe_3$ (x = 0, 0.25%, 0.5%, 1%, 2%) are shown in Fig. 1(d). As illustrated, the diffraction peaks of $CuCd_{(1+x)}InSe_3$ (x = 0, 0.25%, 0.5%, 1%, 2%) can be well indexed to the cubic zinc blende structure with a space group of $F(\bar{4}3m)$, and no secondary phase was detected within the sensitivity of the instrument.

The optical band gap E_g, the Debye temperature θ_D, the electrical conductivity σ, the carrier concentration n, the mobility μ, the Seebeck coefficient α and the lattice thermal conductivity κ_L.

The optical band gap and thermoelectric transport parameters at room temperature for CdSe, $CuInSe_2$ and $CuCdInSe_3$ are exhibited in Table 1. Fig. S1 displays the infrared spectroscopy measurement and optical band gap of the $CuCd_{(1+x)}InSe_3$ (x = 0, x = 0.5%) at room temperature. This figure illustrates that the optical band gap of $CuCdInSe_3$ is about 0.7 eV, which is narrower than that of the CdSe and $CuInSe_2$ reported in the literature [31,32]. The carrier concentration of $CuCdInSe_3$ at room temperature is 3.8×10^{16} cm^{-3}, which is higher than that of CdSe and $CuInSe_2$. The carrier mobility of $CuCdInSe_3$ at room temperature is 365.2 cm^2 V^{-1} s^{-1}. In addition, the lattice thermal

Table 1
Summary of the room temperature transport parameters derived from optical and thermoelectric measurements for CdSe, $CuInSe_2$ and $CuCdInSe_3$.

Parameters	CdSe	$CuInSe_2$	$CuCdInSe_3$
Crystalline phase	Wurtzite/ Hexagonal	Chalcopyrite/ Tetragonal	Zinc blende/ Cubic
Space group	$P6_3/mc$	$I\bar{4}2d$	$F\bar{4}3m$
E_g [eV]	1.74 [31]	1.04 [32]	0.70
Transition type	Direct [33]	Direct	Indirect
Semiconductor type	n	p	p
θ_D [K]	281.7	239.5	264.6
σ [S m^{-1}]	2.3×10^{-3}	2.3×10^{2}	2.2×10^{2}
n [cm^{-3}]	2.7×10^{11}	1.7×10^{16}	3.8×10^{16}
μ [cm^2 V^{-1} s^{-1}]	521.9	849.8	365.2
α [μV K^{-1}]	−1250.5	598.6	197.1
κ_L [Wm^{-1}K^{-1}]	7.2	5.0	2.3

conductivity of $CuCdInSe_3$ is 2.3 Wm^{-1}K^{-1} at room temperature, which is considerably lower than that of CdSe ($\kappa_L = 7.2$ Wm^{-1}K^{-1}) and $CuInSe_2$ ($\kappa_L = 5.0$ Wm^{-1}K^{-1}). It is found that $CuCdInSe_3$ is a novel semiconductor material with low carrier concentration, high mobility and low lattice thermal conductivity. It is expected that the carrier concentration and mobility of $CuCdInSe_3$ can be tuned by doping to obtain superior thermoelectric properties.

We also investigated the thermal stability and composition uniformity of the $CuCdInSe_3$ compounds. The heat flow curve of $CuCdInSe_3$ is

Table 2
The fitting parameters of the low-temperature heat capacity for CdSe, $CuInSe_2$ and $CuCdInSe_3$ by Debye-Einstein model. Here, b is the Debye lattice term, A_i and θ_{Ei} are the amplitude and the Einstein temperature of the ith Einstein oscillator mode, and θ_D is the Debye temperature.

Parameters	CdSe	$CuInSe_2$	$CuCdInSe_3$
b [mJ mol^{-1} K^{-4}]	0.04	0.02	0.07
A_1	0.60	23.40	2.02
θ_{E1} [K]	24.46	66.59	35.45
A_2	14.91	38.39	38.79
θ_{E2} [K]	59.25	153.73	69.65
θ_D [K]	315.4	245.8	270.7

shown in Fig. S2. It can be seen from the figure that there is no second-phase precipitation or phase transformation in the $CuCdInSe_3$ at temperatures ranging from 300 K to 1073 K, indicating that the compound is thermally stable. Fig. S3 (a-d) presents the back-scattering electron images and element distribution maps by EDS on the polished surfaces of $CuCdInSe_3$ and $CuCd_{1.005}InSe_3$, respectively. It shows a uniform distribution of elements in the sample, and no obvious enrichment or absence of elements was observed. In addition, more than five micro-regions were arbitrarily selected for quantitative EDS analysis for each element. The results of the quantitative EDS analysis show that the components of $CuCdInSe_3$ and $CuCd_{1.005}InSe_3$ are consistent with the stoichiometric ratios (Table S1).

Fig. S4 shows high-resolution X-ray photoelectron spectra (XPS) of $CuCdInSe_3$. Due to the charge effect, the core-level electron binding energy for each element in the sample was corrected based on the C-1s photoelectron peak at 284.8 eV. In the Cu-2p spectrum (Fig. S4(a)), one notes that there are two peaks located at 952.3 eV and 932.4 eV, corresponding to Cu-2p1/2 and Cu-2p3/2, respectively. The energy position of Cu-2p matches well with the Cu-2p orbital of Cu_2S [34]. Fig. S4(b) is the spectrum of the Cd-3d core state. The binding energies of Cd-3d3/2 and Cd-3d5/2 are 412.0 eV and 405.2 eV, respectively, corresponding to the Cd-3d orbitals of CdSe [34]. Fig. S4(c) shows the spectrum of the In-3d core state and the binding energies of the In-3d3/2 and In-3d5/2 are 452.5 eV and 444.9 eV. The energy position of In-3d matches well with the In-3d orbitals of $CuInSe_2$ or In_2Se_3 [35,36]. The binding energy of the Se-3d core state is 54.1 eV, corresponding to the Se-3d orbital of CdSe or In_2Se_3, Fig. S4(d) [34,36]. We can identify that Cu, Cd, In and Se are in the Cu^+ state, Cd^{2+} state, In^{3+} state, and Se^{2-} state in the $CuCdInSe_3$, respectively.

To investigate the microstructure and composition of the $CuCdInSe_3$ compound, the $CuCdInSe_3$ TEM specimen preparation was done by using Focused Ion Beam (FIB) technique, followed by S/TEM and EDS analysis. The TEM bright field image of the $CuCdInSe_3$, shown in Fig. 2 (a), reveals a clean grain interior without any second phase. The selected area electron diffraction (SAED) pattern in Fig. 2(b) confirms the presence of a cubic zinc blende structure, captured along the [011] zone axis. To further determine the crystal structure, SAED patterns of single crystals with various zone axes were collected, as presented in Fig. S5. These patterns were simulated and analyzed using Landyne software [37], and the results were consistent with the cubic zinc blende structure observed in previous XRD refinement findings.

Fig. 2(c) presents an atomic resolution Cs-corrected high-angle annular dark field in scanning transmission electron microscopy (HAADF-STEM) image of $CuCdInSe_3$, acquired along the [011] zone axis. The cation Cu/Cd/In, which randomly occupies the same cationic site, forms a dumbbell structure with the anion Se. These dumbbell structures stack in the typical ABC/ABC sequence, representative of a zinc blende structure. Additionally, atomic STEM EDS analysis was conducted to examine the atomic-scale homogeneity of the compound (Fig. 2(d-g)). The analysis revealed a homogeneous distribution of the four elements at the nanometer scale. The atomic lattices and positions

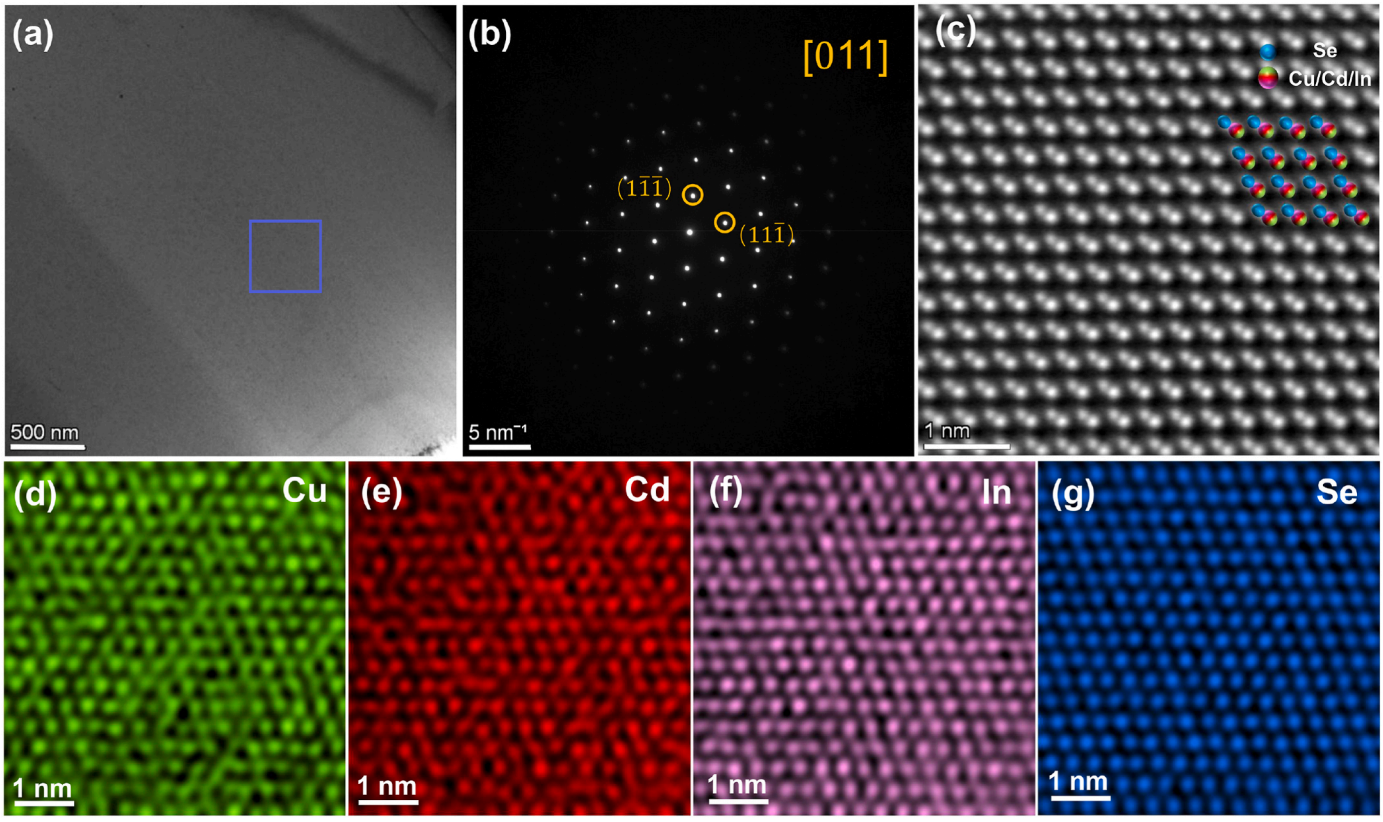

Fig. 2. S/TEM analyses of $CuCdInSe_3$ sample. (a) TEM image of $CuCdInSe_3$; (b) Selected area electron diffraction (SAED) pattern of the figure (a); (c) Cs-corrected HAADF-STEM image; (d–g) Atomic EDS mapping of Cu, Cd, In and Se in $CuCdInSe_3$.

of each element were clearly discernible, indicating the compound's stable atomic arrangement order and structure.

3.2. Electronic band structure

First-principles DFT calculations are performed using QUANTUM ESPRESSO [38,39] package with GBRV ultrasoft pseudopotentials [40]. The structures are fully optimized using generalized gradient approximation of Perdew–Burke–Ernzerhof revised for solid (PBEsol) type [41]. As a benchmark study, we first study the electronic structure of CdSe using a supercell of 24 atoms with the structural parameters fully optimized using a 4 × 4 × 1 Monkhorst-Pack *k*-point grid for Brillouin zone sampling, an energy convergence threshold of 10^{-6} Ry, and a force convergence threshold of 10^{-5} Ry/Bohr. The plane-wave cutoff is set to 50 Ry and the charge density cutoff is set to 250 Ry, respectively. It is well known that (semi-)local density functional like PBEsol often underestimates the band gap, we also adopt the newly developed pseudohybrid Hubbard density functional, Agapito-Curtarolo-Buongiorno Nardelli (ACBN0) which is a DFT+*U* method with the on-site Coulomb repulsion *U* value determined self-consistently [42]. Following the implementation in Ref. [43], we compute the ACBN0 band structure of CdSe, with the comparison to the PBEsol band structure shown in Fig. S6. It is evident that ACBN0 predicts a band gap of 1.564 eV, a substantial improvement over the PBEsol value of 0.632 eV.

We further investigate the electronic structure of $CuCdInSe_3$ solid solutions with ACBN0. A 3 × 3 × 2 supercell of 108 atoms is used to model a single grain (SG) with configurations generated using the Supercell program [44]. We select one configuration that has dopants nearly homogeneously distributed in the supercell and then optimize the structure using PBEsol with the plane-wave cutoff, charge density cutoff, and *k*-point grid set to 50 Ry, 250 Ry, and 4 × 4 × 1, respectively. The electronic band structure of $CuCdInSe_3$ with ACBN0 is presented in Fig. 3(a). Fig. 3(b) demonstrates the first Brillouin zone of the $CuCdInSe_3$ compound with a cubic structure with the path of Γ-M-K-Γ-A [45]. The $CuCdInSe_3$ compound has a semiconducting electronic structure with a narrow-band gap between the valence band (VB) and the conduction band (CB). The calculated band gap is 0.0038eV. It should be noted that the large difference between the optical bandgap value and the DFT-predicted value is probably due to the strong interference in absorption caused by the large population of free carriers [23,46]. The bottom of the conduction band is relatively flat at Γ point, and significant energy shifts of valence bands caused the relocation of the valence band maximum between Γ and A. Electronic density of states for $CuCdInSe_3$ compound is also shown in Fig. 3(a). The density of the total electron states increases rapidly as the Fermi level goes deeper into the valence band. The top valence band edges of $CuCdInSe_3$ compounds are mainly composed of Se-4p and Cu-3d orbitals, and the bottom conduction band edges are mainly derived from Se-4p and In-5s orbitals.

3.3. Electrical transport properties

Fig. 4 displays the electrical transport properties as a function of temperature for $CuCd_{(1+x)}InSe_3$ (x = 0–2%). The electrical conductivity σ of the samples enhance with the Cd doping elevated. $CuCd_{(1+x)}InSe_3$ (x = 0.5–2%) samples exhibit a typical degenerate semiconductor behavior in the temperature range of 300~780 K, where the electrical conductivity decreases with rising temperature (Fig. 4(a)). $CuCdInSe_3$ has a low electrical conductivity of ~220 Sm^{-1} at room temperature owing to its low carrier concentration. The poor electrical conductivity is largely improved by Cd doping and reaches ~3.99 × 10^4 Sm^{-1} at room temperature for $CuCd_{1.02}InSe_3$.

The temperature dependence of the Seebeck coefficient for the $CuCd_{(1+x)}InSe_3$ (x = 0–2%) is shown in Fig. 4(b). The intrinsic $CuCdInSe_3$ exhibits p-type conduction near room temperature and a p-n transition occurs as the temperature is gradually raised to 323 K. The Seebeck coefficients of $CuCd_{(1+x)}InSe_3$ (x = 0.25–2%) are all negative, indicating that electrons are the majority carriers for transport over the entire temperature range, which is consistent with the Hall measurement results as shown in Fig. S7. With the increase of Cd, Seebeck coefficient of $CuCd_{(1+x)}InSe_3$ (x = 0.25–2%) decreases from −120.18 to −84.56 μV K^{-1} at room temperature.

We also performed low-temperature Hall measurements to characterize the temperature dependence of carrier mobility and concentration. The carrier concentration of $CuCd_{(1+x)}InSe_3$ (x = 0–2%) in the temperature range of 10~300 K is shown in Fig. 4(c). The carrier concentration gradually increases with Cd doping and is nearly independent of temperature for all samples, indicating a highly degenerate semiconducting behavior. The carrier concentration increases from 3.77 × 10^{16} cm^{-3} for $CuCdInSe_3$ to 1.09 × 10^{19} cm^{-3} for $CuCd_{1.02}InSe_3$ with doping Cd.

Fig. 4(d) exhibits the carrier mobility for $CuCd_{(1+x)}InSe_3$ (x = 0.5%) as a function of temperature. The carrier mobility of $CuCd_{(1+x)}InSe_3$ (x = 0–2%) at low temperatures (10–90 K) follow a typical $\mu \sim T^0$ temperature dependence, indicating that neutral impurity scattering plays a dominant role. The lattice vibration increases and the carrier mobility decreases gradually with the rising temperature (90–200 K), satisfying the $\mu \sim T^{-1/2}$ relationship, indicating that the alloying scattering begins to strengthen with the increase of Cd doping, and the carriers are mainly affected by alloying scattering and acoustic phonon scattering. The carrier mobility of $CuCd_{(1+x)}InSe_3$ (x = 0.25–2%) in the temperature range of 200~300 K follow a typical $\mu \sim T^{-3/2}$ temperature dependence, which means the acoustic phonon scattering is dominate. The carrier mobility of the intrinsic sample in the temperature range of 200~300 K is proportional to $\mu \sim T^{-1/2}$, revealing that the charge carriers are predominantly scattered by a mixture of alloying scattering and acoustic phonon scattering. Cd doping significantly improves the carrier concentration and electrical conductivity. As shown in Fig. 4(e), $CuCd_{1.01}InSe_3$ exhibits a highest power factor 0.58 $mWm^{-1}K^{-2}$ at 578 K,

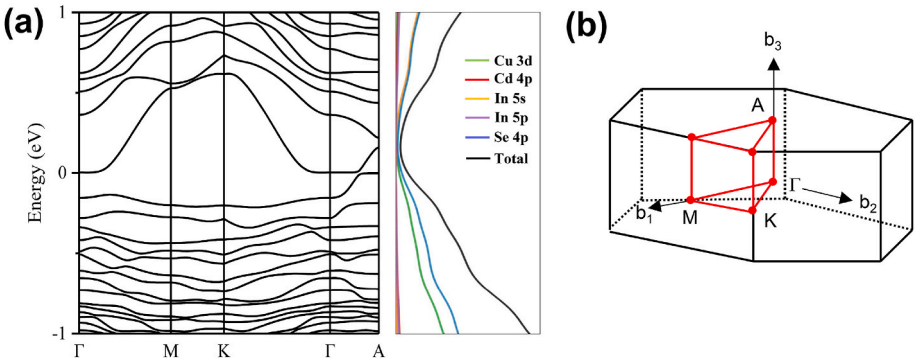

Fig. 3. (a) Calculated electronic band structure and the corresponding projected density of states of $CuCdInSe_3$ compound. (b) Brillouin zone of cubic structure with the path of Γ-M-K-Γ-A.

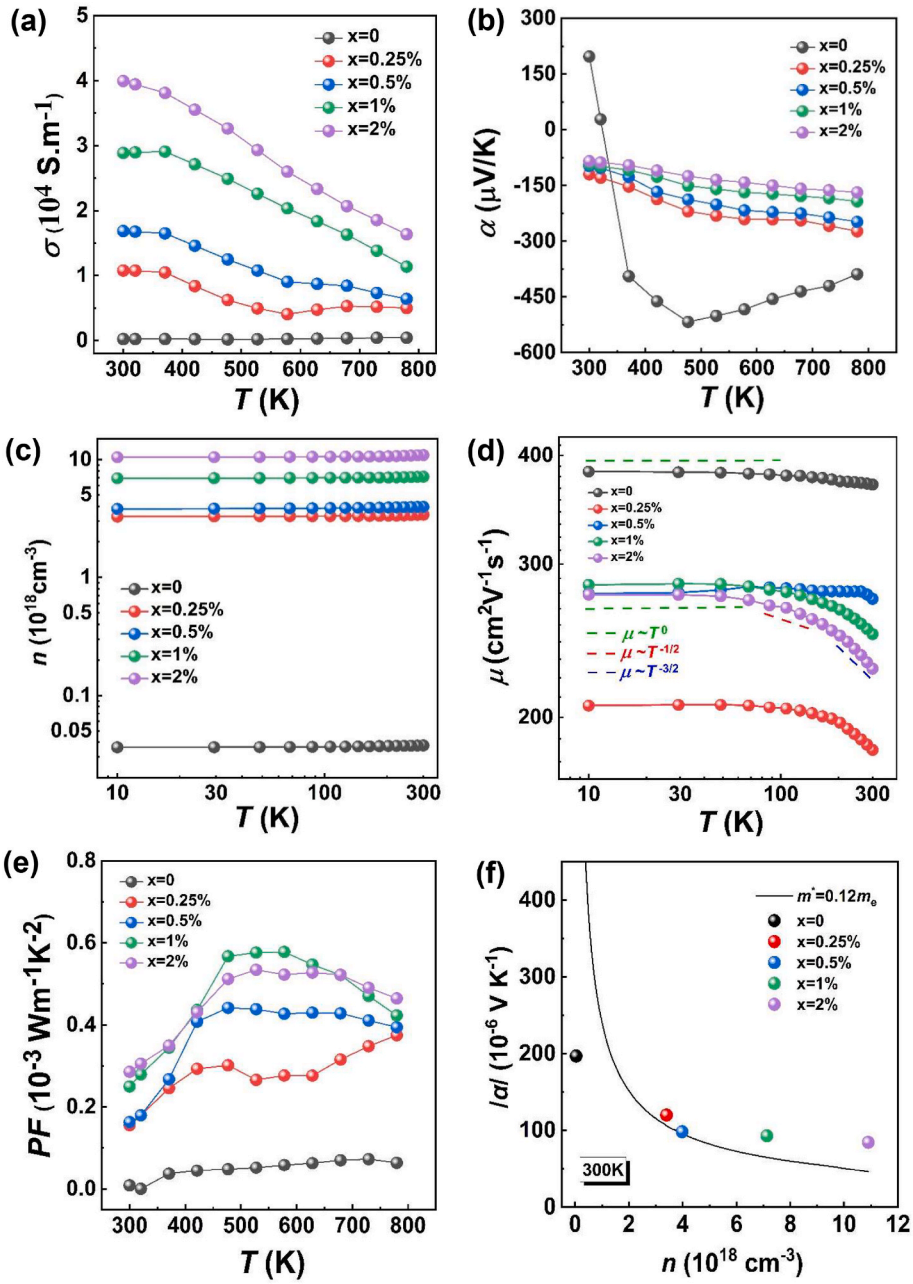

Fig. 4. Electrical transport properties as a function of temperature for $CuCd_{(1+x)}InSe_3$ (x = 0–2%). (a) electrical conductivity, σ; (b) Seebeck coefficient, α; (c) Carrier concentration in the temperature range of 10~300 K; (d) Carrier mobility in the temperature range of 10~300 K (The green dashed line with T^0 dependence represents the dominant neutral impurity scattering, the red dashed line with $T^{-1/2}$ dependence represents the dominant alloying scattering accompanied by acoustic phonon scattering, and the blue dashed line with $T^{-3/2}$ dependence represents the dominant acoustic phonon scattering); (e) Power factor;*PF* (f) Room temperature Seebeck coefficient as a function of the carrier concentration, so-called Pisarenko plot (the solid black line is the fitted line with effective mass of 0.12 m_e and the predominant acoustic phonon scattering).

which is about 9.6 times higher than that of the $CuCdInSe_3$ (0.06 $mWm^{-1}K^{-2}$) at 578 K.

Fig. 4(f) plots the Seebeck coefficient as a function of the carrier concentration (Pisarenko curve) for $CuCd_{(1+x)}InSe_3$. With the assumption of a single parabolic band model and dominated acoustic phonon scattering, the Seebeck coefficient can be expressed as [47]:

$$\alpha = \frac{8\pi^2 k_B^2 m^* T(\pi/3n)^{2/3}}{3eh^2} \quad (1)$$

here, α is the Seebeck coefficient, k_B is the Boltzmann constant, n is the carrier concentration, and m^* is the effective mass, h is the Planck constant, e is the elemental electron charge. As shown in Table S2, the intrinsic sample has a tiny effective carrier mass of 0.01 m_e. With Cd doping, the effective mass of the sample gradually increases, which enhances the carrier concentration but suppresses the mobility. The $CuCd_{1.005}InSe_3$ with the highest thermoelectric property has an effective mass of 0.12 m_e. The carrier concentration significantly increases from 3.77×10^{16} cm^{-3} to 3.98×10^{18} cm^{-3} at room temperature, and the mobility declines from 365.2 $cm^2 V^{-1} s^{-1}$ to 264.4 $cm^2 V^{-1} s^{-1}$.

3.4. Thermal transport properties

Total thermal conductivity as a function of temperature for $CuCd_{(1+x)}InSe_3$ (x = 0–2%) is shown in Fig. 5(a). The thermal conductivity of $CuCd_{(1+x)}InSe_3$ (x = 0–2%) declines with the increasing temperature. $CuCdInSe_3$ exhibits a relatively low thermal conductivity of 2.29 $Wm^{-1}K^{-1}$ at 300 K, ~50% lower than that of $CuInSe_2$ (5.02 $Wm^{-1}K^{-1}$) at room temperature. With the rising temperature, the thermal conductivity of $CuCdInSe_3$ descends to 0.76 $Wm^{-1}K^{-1}$ at 780 K.

The improved electrical properties integrating with the low thermal conductivity result in an enhanced figure-of-merit *ZT* value of 0.45 at 780 K for $CuCd_{1.005}InSe_3$, which is seven times higher than that of the pristine $CuCdInSe_3$(ZT_{max} ~ 0.06@780 K) (Fig. 5(b)).

To further investigate the low thermal conductivity transport

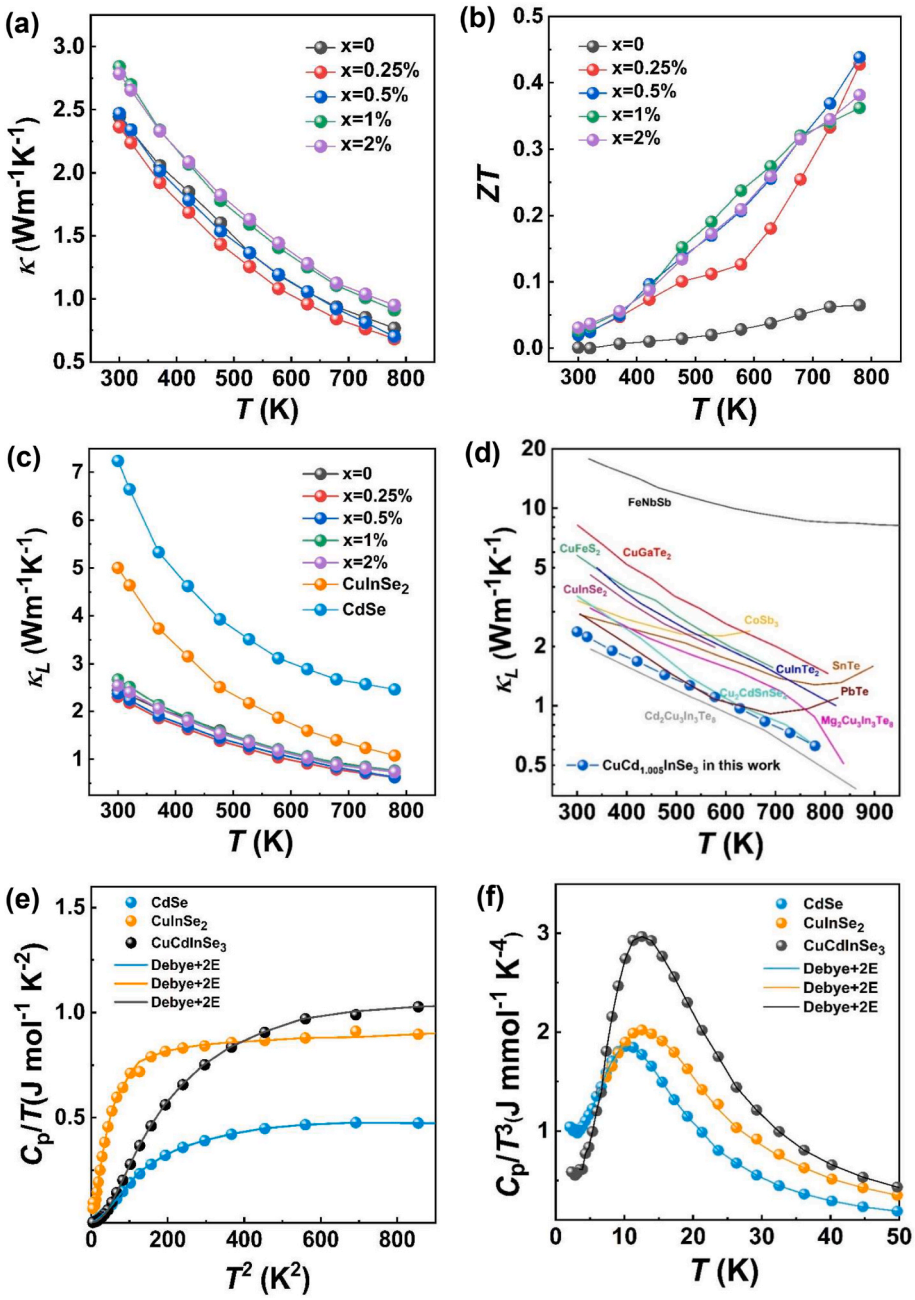

Fig. 5. (a) Total thermal conductivity as a function of temperature for $CuCd_{(1+x)}InSe_3$ (x = 0–2%). (b) Figure of merit *ZT* values of $CuCd_{(1+x)}InSe_3$ (x = 0–2%). (c) Lattice thermal conductivity as a function of temperature for $CuCd_{(1+x)}InSe_3$ (x = 0–2%). (d) Lattice thermal conductivity as a function of temperature for $CuCdInSe_3$ in comparison with some traditional thermoelectric materials. (e) C_p/T as a function of T^2 in a range of 4~300 K (here, C_p is the heat capacity). The solid line is calculated by using the combined Debye-2Einstein model. (f) The specific heat plotted as C_p/T^3 versus T and the solid lines are the fitting results of the Debye-2Einstein model. The fitting parameters are presented in Table 2.

mechanism of $CuCdInSe_3$-based compounds, the lattice thermal conductivity of $CuCd_{(1+x)}InSe_3$ (x = 0–2%) was calculated as a function of temperature, as shown in Fig. 5(c). The lattice thermal conductivity of each sample descends with the increasing temperature, which is mainly due to the intensify of U scattering and the scattering of heat-carrying phonons. It can be seen from the previous electrical transport results that the bipolar thermal conductivity of $CuCd_{(1+x)}InSe_3$ (x = 0–2%) contributes little to the total thermal conductivity in the temperature range of 300~780 K, where the bipolar thermal conductivity is approximately 0. Therefore, the lattice thermal conductivity can be obtained from the Wiedemann-Franz law [48,49]:

$$\kappa_L = \kappa\text{-}\kappa_e \tag{2}$$

$$\kappa_e = L\sigma T \tag{3}$$

where κ_L is the lattice thermal conductivity, κ is the total thermal conductivity, κ_e is the electronic thermal conductivity, σ is the electrical conductivity, and L is the Lorentz constant, respectively. Assuming that the electronic band structure is approximated by a single parabolic band model, the Lorentz constant L can be calculated by the following formula [50,51]:

$$L = \left(\frac{k_B}{e}\right)^2 \left(\frac{(r+7/2)F_{r+5/2}(\eta)}{(r+3/2)F_{r+1/2}(\eta)} - \left[\frac{(r+5/2)F_{r+3/2}(\eta)}{(r+3/2)F_{r+1/2}(\eta)}\right]^2\right) \tag{4}$$

The reduced Fermi level η can be obtained by equations (5) and (6) :

$$\alpha = \pm\frac{k_B}{e}\left[\frac{(r+5/2)F_{r+3/2}(\eta)}{(r+3/2)F_{r+1/2}(\eta)} - \eta\right] \tag{5}$$

$$F_n(\eta) = \int_0^\infty \frac{\chi^n}{1+e^{\chi-\eta}} d\chi \tag{6}$$

Here, α is the Seebeck coefficient, k_B represents the Boltzmann constant, e is the electron charge, and r is the scattering factor. Since the

charge carriers are scattered mainly by acoustic phonons, the scattering factor r is taken to be −1/2. The results of lattice thermal conductivity are shown in Fig. 5(c) and Table S2. The $CuCd_{(1+x)}InSe_3$ (x = 0.5%) obtained a lower lattice thermal conductivity (0.62 $Wm^{-1}K^{-1}$ @ 780 K) than that of $CuCdInSe_3$ (0.78 $Wm^{-1}K^{-1}$ @ 780 K).

Fig. 5(d) shows the lattice thermal conductivity as a function of temperature for $CuCdInSe_3$ in comparison with some traditional thermoelectric materials, including SnTe [52], PbTe [1], $CoSb_3$ [53], FeNbSb [54], $CuFeS_2$ [55], $CuInSe_2$ [35], $CuInTe_2$ [56], $CuGaTe_2$ [57], $Cu_2CdSnSe_4$ [58], $Mg_2Cu_3In_3Te_8$ [59], $Cd_2Cu_3In_3Te_8$ [60]. The lattice thermal conductivity of $CuCdInSe_3$ is much lower than the Cu-based diamond-like compounds such as $CuFeS_2$ [55], $CuInSe_2$ [35], $CuInTe_2$ [56], $CuGaTe_2$ [57], $Cu_2CdSnSe_4$ [58]. In addition, Cu-based materials such as Cu_2Q (Q = S, Se, Te) have the structural characteristics of "electronic crystal-phonon liquid", although these liquid compounds have excellent thermoelectric properties, in the presence of external electric or temperature fields, the cations inside the material are prone to migration, enrichment, or precipitation, thereby reducing their thermal stability and service stability. The cations in $CuCdInSe_3$ are randomly disordered, leading to strong alloy scattering, which can effectively scatter thermal phonons and result in a low lattice thermal conductivity. Meanwhile, the thermal stability of $CuCdInSe_3$ is better than most of the liquid compounds, which is important for TE device applications.

To give further insight into the differences in thermal transport of CdSe, $CuInSe_2$ and $CuCdInSe_3$, the low-temperature heat capacities of the three compounds were measured from 4 K to 300 K, as displayed in Fig. 5(e-f). As the temperature rises, more phonon modes are excited and the heat capacity of the three compounds steadily increases. The Dulong–Petit limiting value is 98.3 J mol^{-1} K^{-1} for $CuCdInSe_3$ at 300 K.

The low-temperature heat capacity of CdSe, $CuInSe_2$ and $CuCdInSe_3$ from 4 K to 300 K can be well fitted by the Debye-Einstein model, and the $C_p/T \sim T^2$ relation can be fitted well by the Debye-2Einstein model:

$$\frac{C_P}{T} = \gamma + bT^2 + \sum_{i=1}^{n}\left(A_i(\theta_{Ei})^2 \cdot \left(T^2\right)^{-3/2} \cdot \frac{e^{\theta_{Ei}/T}}{\left(e^{\theta_{Ei}/T}-1\right)^2}\right) \quad (7)$$

The first term γ in Equation (7) represents the contribution from electrons that is the Sommerfeld constant given by Equation (8):

$$\gamma = \frac{\pi^2}{3}k_B^2 N(E_F) = 1.36\times10^{-4}\times V_{mol}^{2/3} n_\gamma^{1/3}\frac{m^*}{m_0} \quad (8)$$

where V_{mol} is the molar volume, n_γ is the number of electrons in the cell, and m^*/m_0 is the effective mass, respectively.

The second term bT^2 represents the lattice contribution to the heat capacity, which can be expressed as follows :

$$b = C\cdot\left(12\pi^4 N_A k_B\right) / \left(5\theta_D^3\right) \quad (9)$$

where θ_D is the Debye temperature, N_A is Avogadro constant, and k_B is Boltzmann's constant. The parameter C can be expressed as:

$$C = 1 - \sum_i A_i \Big/ 3NR \quad (10)$$

Here, N is the number of atoms per unit cell, R is the gas constant. The third term represents the contribution of the Einstein harmonic oscillator to the heat capacity, A_i and θ_{Ei} are the amplitude and the Einstein temperature of the ith Einstein oscillator mode. By fitting $C_p/T \sim T^2$, the A_i, θ_{Ei}, θ_D, γ and b can be obtained from the slope and intercept of the line. The results of relevant parameters are shown in Table 2.

It has been shown that the boson peak is typically ascribed to an excess density of vibrational states, and the frequency of the boson peak is equal to the Ioffe-Regel limit of the "transverse" phonon, beyond which the transverse phonon no longer propagates [61]. The origin of the boson peak is transverse vibrational modes associated with defective soft structures in the disordered state. The increasing disorder leads to the generation of boson peak whose height increases with increasing defect concentration [61,62]. In this work, the Cu/Cd/In cations in $CuCdInSe_3$ are randomly disordered, and the cation disorder is higher than that of the binary CdSe and ternary $CuInSe_2$ compounds. We adopt the Debye-2 Einstein model to fit the low-temperature heat capacity. Boson peaks of CdSe, $CuInSe_2$ and $CuCdInSe_3$ are observed in the C_p/T^3-T curves, which are raised with the increasing composition, as shown in Fig. 5(f).

In addition, the transverse and longitudinal wave velocities of CdSe, $CuInSe_2$ and $CuCdInSe_3$ were measured by the pulse-echo method. The results of Young's modulus E, Poisson's ratio V_p, shear modulus G and Grueneissen parameter γ of the samples were listed in Table 3. As can be seen from Table 3, the lattice thermal conductivity of $CuCdInSe_3$ is 2.29 $Wm^{-1}K^{-1}$ at room temperature, which is much lower than $CuInSe_2$ and CdSe. The Young's modulus and shear modulus of $CuCdInSe_3$ are closed to that of $CuInSe_2$ and are larger than CdSe, indicating greater rigidity for $CuCdInSe_3$ and $CuInSe_2$. It is shown that the low lattice thermal conductivity for $CuCdInSe_3$ compound is mainly due to the alloying scattering.

4. Conclusions

In summary, we report the thermoelectric performance and electronic band structure of $CuCdInSe_3$ compound with stable cubic zinc blende structure for the first time by entropy modulation via alloying $CuInSe_2$ with CdSe. This entropy driven order-disorder transition on the cation site, combined with the alloying scattering, leads to a low thermal conductivity for $CuCdInSe_3$. Furthermore, we explored the impact of excess Cd in $CuCd_{(1+x)}InSe_3$ compounds, which resulted in optimized carrier concentration and power factor. Notably, the sample $CuCd_{(1+x)}InSe_3$ (x = 0.5%) achieved a maximum ZT value of 0.45 at 780 K. Among the n-type Cu-based diamond-like thermoelectric materials reported to date, this compound has demonstrated exceptional performance. Its outstanding characteristics suggest great potential for applications in thermoelectric materials and devices, marking a significant advancement in the field.

CRediT authorship contribution statement

Tingting Luo: Data curation, Writing – original draft. **Yihao Hu:** Data curation, Writing – review & editing. **Shi Liu:** Conceptualization, Writing – review & editing. **Fanjie Xia:** Investigation. **Junhao Qiu:** Investigation. **Haoyang Peng:** Data curation. **Keke Liu:** Data curation. **Quansheng Guo:** Writing – review & editing. **XingZhong Li:** Data curation, Writing – review & editing. **Dongwang Yang:** Data curation. **Xianli Su:** Conceptualization, Funding acquisition, Writing – review & editing. **Jinsong Wu:** Supervision, Funding acquisition, Writing – review & editing. **Xinfeng Tang:** Conceptualization, Supervision, Writing – review & editing, Funding acquisition.

Table 3
Experimental data of lattice thermal conductivity κ_L, sound velocity (V_S is the transverse sound velocity, V_l is the longitudinal sound velocity, V_a is the average sound velocity) and the calculated elastic properties (V_p is the Poisson ratio, E is the Young's modulus, G is the Shear modulus, γ is Grüeneissen parameter, and θ_D is the Debye temperature).

Parameters	CdSe	$CuInSe_2$	$CuCdInSe_3$
κ_L [$Wm^{-1}K^{-1}$]	7.24	5.02	2.29
V_S [m s^{-1}]	1622	1982	1845
V_l [m s^{-1}]	3680	4143	3966
V_a [m s^{-1}]	1831	2229	2077
V_p	0.38	0.35	0.36
E [GPa]	42.17	58.94	52.84
G [GPa]	15.29	21.81	19.40
γ	2.40	2.14	2.24
θ_D [K]	281.7	239.5	264.6

Declaration of competing interest

The authors declare that they have no known competing financial interests or personal relationships that could have appeared to influence the work reported in this paper.

Data availability

Data will be made available on request.

Acknowledgements

This work was supported by the National Natural Science Foundation of China (52122108, 51972256, and 52150710537), National Key Research and Development Program of China (Grant No. 2019YFA0704900), and the 111 Project of China (Grant No. B07040).

Appendix A. Supplementary data

Supplementary data to this article can be found online at https://doi.org/10.1016/j.mtphys.2023.101211.

References

[1] Y. Pei, X. Shi, A. LaLonde, H. Wang, L. Chen, G.J. Snyder, Convergence of electronic bands for high performance bulk thermoelectrics, Nature 473 (2011) 66–69, https://doi.org/10.1038/nature09996.
[2] X. Shi, L. Chen, C. Uher, Recent advances in high-performance bulk thermoelectric materials, Int. Mater. Rev. 61 (2016) 379–415, https://doi.org/10.1080/09506608.2016.1183075.
[3] J. He, T.M. Tritt, Advances in thermoelectric materials research: looking back and moving forward, Science 357 (2017) 1369, https://doi.org/10.1126/science.aak9997.
[4] Y.K. Yang, H.Y. Chen, D.M. Li, D.Q. Yuan, B. Zheng, S. Yu, G.T. Zou, The growth of PbTe on H-terminated Si(111) substrate by hot wall epitaxy, Infrared Phys. Technol. 44 (2003) 299–301, https://doi.org/10.1016/S1350-4495(02)00228-1.
[5] L.D. Zhao, V.P. Dravid, M.G. Kanatzidis, The panoscopic approach to high performance thermoelectrics, Energy Environ. Sci. 7 (2014) 251–268, https://doi.org/10.1039/c3ee43099e.
[6] M. Hong, J. Zou, Z.G. Chen, Thermoelectric GeTe with diverse degrees of freedom having secured superhigh performance, Adv. Mater. 31 (2019): e1807071, https://doi.org/10.1002/adma.201807071.
[7] J. Dong, F.-H. Sun, H. Tang, J. Pei, H.L. Zhuang, H.H. Hu, B.P. Zhang, Y. Pan, J. F. Li, Medium-temperature thermoelectric GeTe: vacancy suppression and band structure engineering leading to high performance, Energy Environ. Sci. 12 (2019) 1396–1403, https://doi.org/10.1039/c9ee00317g.
[8] Y. Tang, Z.M. Gibbs, L.A. Agapito, G. Li, H.S. Kim, M.B. Nardelli, S. Curtarolo, G. J. Snyder, Convergence of multi-valley bands as the electronic origin of high thermoelectric performance in CoSb3 skutterudites, Nat. Mater. 14 (2015) 1223–1228, https://doi.org/10.1038/nmat4430.
[9] X. Tang, Z. Li, W. Liu, Q. Zhang, C. Uher, A comprehensive review on Bi_2Te_3-based thin films: thermoelectrics and beyond, Interdisciplinary Materials 1 (2022) 88–115, https://doi.org/10.1002/idm2.12009.
[10] G. Zheng, X. Su, T. Liang, Q. Lu, Y. Yan, C. Uher, X. Tang, High thermoelectric performance of mechanically robust n-type $Bi_2Te_{3-x}Se_x$ prepared by combustion synthesis, J. Mater. Chem. A 3 (2015) 6603–6613, https://doi.org/10.1039/c5ta00470e.
[11] Z. Zheng, X. Su, R. Deng, C. Stoumpos, H. Xie, W. Liu, Y. Yan, S. Hao, C. Uher, C. Wolverton, M.G. Kanatzidis, X. Tang, Rhombohedral to cubic conversion of GeTe via MnTe alloying leads to ultralow thermal conductivity, electronic band convergence, and high thermoelectric performance, J. Am. Chem. Soc. 140 (2018) 2673–2686, https://doi.org/10.1021/jacs.7b13611.
[12] Z. Liu, T. Hong, L. Xu, S. Wang, X. Gao, C. Chang, X. Ding, Y. Xiao, L.D. Zhao, Lattice expansion enables interstitial doping to achieve a high average ZT in n-type PbS, Interdisciplinary Materials 2 (2022) 161–170, https://doi.org/10.1002/idm2.12056.
[13] J. Zhang, D. Wu, D. He, D. Feng, M. Yin, X. Qin, J. He, Extraordinary thermoelectric performance realized in n-type PbTe through multiphase nanostructure engineering, Adv. Mater. 29 (2017): 1703148, https://doi.org/10.1002/adma.201703148.
[14] M. Hong, Z.G. Chen, L. Yang, J. Zou, Enhancing thermoelectric performance of Bi2Te3-based nanostructures through rational structure design, Nanoscale 8 (2016) 8681–8686, https://doi.org/10.1039/c6nr00719h.
[15] Y. Zheng, Q. Zhang, X. Su, H. Xie, S. Shu, T. Chen, G. Tan, Y. Yan, X. Tang, C. Uher, G.J. Snyder, Mechanically robust BiSbTe alloys with superior thermoelectric performance: a case study of stable hierarchical nanostructured thermoelectric materials, Adv. Energy Mater. 5 (2015), https://doi.org/10.1002/aenm.201401391.
[16] D.Z. Wang, W.D. Liu, M. Li, K. Zheng, H. Hu, L.C. Yin, Y. Wang, H. Zhu, X.L. Shi, X. Yang, Q. Liu, Z.G. Chen, Hierarchical architectural structures induce high performance in n-type GeTe-based thermoelectrics, Adv. Funct. Mater. 33 (2023), https://doi.org/10.1002/adfm.202213040.
[17] L. Hu, T. Zhu, X. Liu, X. Zhao, Point defect engineering of high-performance bismuth-telluride-based thermoelectric materials, Adv. Funct. Mater. 24 (2014) 5211–5218, https://doi.org/10.1002/adfm.201400474.
[18] L. Xie, R. Liu, C. Zhu, Z. Bu, W. Qiu, J. Liu, F. Xu, Y. Pei, S. Bai, L. Chen, Enhanced thermoelectric performance in $Ge_{0.955-x}Sb_xTe/FeGe_2$ composites enabled by hierarchical defects, Small 17 (2021): e2100915, https://doi.org/10.1002/smll.202100915.
[19] B.B. Jiang, Y. Yu, J. Cui, X.X. Liu, L. Xie, J.C. Liao, Q.H. Zhang, Y. Huang, S.C. Ning, B.H. Jia, B. Zhu, S.Q. Bai, L.D. Chen, S.J. Pennycook, J.Q. He, High-entropy-stabilized chalcogenides with high thermoelectric performance, Science 371 (2021) 830–834, https://doi.org/10.1126/science.abe1292.
[20] Z. Zhang, K. Zhao, H. Chen, Q. Ren, Z. Yue, T.-R. Wei, P. Qiu, L. Chen, X. Shi, Entropy engineering induced exceptional thermoelectric and mechanical performances in $Cu_{2-y}Ag_yTe_{1-2x}S_xSe_x$, Acta Mater. 224 (2022): 11752, https://doi.org/10.1016/j.actamat.2021.117512.
[21] T. Zhao, H. Zhu, B. Zhang, S. Zheng, N. Li, G. Wang, G. Wang, X. Lu, X. Zhou, High thermoelectric performance of tellurium-free n-type $AgBi_{1-x}Sb_xSe_2$ with stable cubic structure enabled by entropy engineering, Acta Mater. 220 (2021): 117291, https://doi.org/10.1016/j.actamat.2021.117291.
[22] M. Dutta, K. Pal, M. Etter, U.V. Waghmare, K. Biswas, Emphanisis in cubic $(SnSe)_{0.5}(AgSbSe_2)_{0.5}$: dynamical off-centering of anion leads to low thermal conductivity and high thermoelectric performance, J. Am. Chem. Soc. 143 (2021) 16839–16848, https://doi.org/10.1021/jacs.1c08931.
[23] Y. Liu, H. Xie, Z. Li, Y. Zhang, C.D. Malliakas, M. Al Malki, S. Ribet, S. Hao, T. Pham, Y. Wang, X. Hu, R. Dos Reis, G.J. Snyder, C. Uher, C. Wolverton, M. G. Kanatzidis, V.P. Dravid, Unraveling the role of entropy in thermoelectrics: entropy-stabilized quintuple rock salt $PbGeSnCd_xTe_{3+x}$, J. Am. Chem. Soc. 145 (2023) 8677–8688, https://doi.org/10.1021/jacs.3c01693.
[24] Y. Zhou, X. Li, L. Xi, J. Yang, Intrinsic defect study on ternary ABX2 diamond-like thermoelectric materials and analysis of the density of energy function, Journal of Materiomics 7 (2021) 19–24, https://doi.org/10.1016/j.jmat.2020.06.012.
[25] R. Li, X. Li, L. Xi, J. Yang, D.J. Singh, W. Zhang, High-Throughput screening for advanced thermoelectric materials: diamond-like ABX_2 compounds, ACS Appl. Mater. Interfaces 11 (2019) 24859–24866, https://doi.org/10.1021/acsami.9b01196.
[26] J. Zhang, R. Liu, N. Cheng, Y. Zhang, J. Yang, C. Uher, X. Shi, L. Chen, W. Zhang, High-performance pseudocubic thermoelectric materials from non-cubic chalcopyrite compounds, Adv. Mater. 26 (2014) 3848–3853, https://doi.org/10.1002/adma.201400058.
[27] J.E. Rowe, J.L. Shay, Extension of the quasicubic model to ternary chalcopyrite crystals, Phys. Rev. B 3 (1971) 451–453, https://doi.org/10.1103/PhysRevB.3.451.
[28] L.B. McCusker, R.B. Von Dreele, D.E. Cox, D. Louër, P. Scardi, Rietveld refinement guidelines, J. Appl. Crystallogr. 32 (1999) 36–50, https://doi.org/10.1107/s0021889898009856.
[29] K. Momma, F. Izumi, VESTA: a three-dimensional visualization system for electronic and structural analysis, J. Appl. Crystallogr. 41 (2008) 653–658, https://doi.org/10.1107/s0021889808012016.
[30] R. Liu, H. Chen, K. Zhao, Y. Qin, B. Jiang, T. Zhang, G. Sha, X. Shi, C. Uher, W. Zhang, L. Chen, Entropy as a gene-like performance indicator promoting thermoelectric materials, Adv. Mater. 29 (2017): 1702712, https://doi.org/10.1002/adma.201702712.
[31] J. Jasieniak, M. Califano, S.E. Watkins, Size-dependent valence and conduction band-edge energies of semiconductor nanocrystals, ACS Nano 5 (2011) 5888–5902, https://doi.org/10.1021/nn201681s.
[32] S.N. Rashkeev, W.R.L. Lambrecht, Second-harmonic generation of I-III-VI_2 chalcopyrite semiconductors: effects of chemical substitutions, Phys. Rev. B 63 (2001): 165212, https://doi.org/10.1103/PhysRevB.63.165212.
[33] F. Herklotz, E.V. Lavrov, V.V. Melnikov, Substitutional sulfur in CdSe: localized vibrational modes, Phys. Status Solidi B 257 (2020): 2000204, https://doi.org/10.1002/pssb.202000204.
[34] J.F. Moulder, W.F. Stickle, P.E. Sobol, K.D. Bombem, Handbook of X-Ray Photoelectron Spectroscopy, Perkin–Elmer Corporation, United States of America, Eden Prairie, Minnesota, 1992.
[35] J. Yao, N.J. Takas, M.L. Schliefert, D.S. Paprocki, P.E.R. Blanchard, H. Gou, A. Mar, C.L. Exstrom, S.A. Darveau, P.F.P. Poudeu, J.A. Aitken, Thermoelectric properties ofp-type $CuInSe_2$ chalcopyrites enhanced by introduction of manganese, Phys. Rev. B 84 (2011): 075203, https://doi.org/10.1103/PhysRevB.84.075203.
[36] C.H. Ho, C.H. Lin, Y.P. Wang, Y.C. Chen, S.H. Chen, Y.S. Huang, Surface oxide effect on optical sensing and photoelectric conversion of alpha-In_2Se_3 hexagonal microplates, ACS Appl. Mater. Interfaces 5 (2013) 2269–2277, https://doi.org/10.1021/am400128e.
[37] X.Z. Li, SVAT4: a computer program for visualization and analysis of crystal structures, J. Appl. Crystallogr. 53 (2020) 848–853, https://doi.org/10.1107/S1600576720004586.
[38] P. Giannozzi, S. Baroni, N. Bonini, M. Calandra, R. Car, C. Cavazzoni, D. Ceresoli, G.L. Chiarotti, M. Cococcioni, I. Dabo, A. Dal Corso, S. de Gironcoli, S. Fabris, G. Fratesi, R. Gebauer, U. Gerstmann, C. Gougoussis, A. Kokalj, M. Lazzeri, L. Martin-Samos, N. Marzari, F. Mauri, R. Mazzarello, S. Paolini, A. Pasquarello, L. Paulatto, C. Sbraccia, S. Scandolo, G. Sclauzero, A.P. Seitsonen, A. Smogunov, P. Umari, R.M. Wentzcovitch, QUANTUM ESPRESSO: a modular and open-source

software project for quantum simulations of materials, J. Phys. Condens. Matter 21 (2009): 395502, https://doi.org/10.1088/0953-8984/21/39/395502.
[39] P. Giannozzi, O. Andreussi, T. Brumme, O. Bunau, M. Buongiorno Nardelli, M. Calandra, R. Car, C. Cavazzoni, D. Ceresoli, M. Cococcioni, N. Colonna, I. Carnimeo, A. Dal Corso, S. de Gironcoli, P. Delugas, R.A. DiStasio Jr., A. Ferretti, A. Floris, G. Fratesi, G. Fugallo, R. Gebauer, U. Gerstmann, F. Giustino, T. Gorni, J. Jia, M. Kawamura, H.Y. Ko, A. Kokalj, E. Kucukbenli, M. Lazzeri, M. Marsili, N. Marzari, F. Mauri, N.L. Nguyen, H.V. Nguyen, A. Otero-de-la-Roza, L. Paulatto, S. Ponce, D. Rocca, R. Sabatini, B. Santra, M. Schlipf, A.P. Seitsonen, A. Smogunov, I. Timrov, T. Thonhauser, P. Umari, N. Vast, X. Wu, S. Baroni, Advanced capabilities for materials modelling with Quantum ESPRESSO, J. Phys. Condens. Matter 29 (2017): 465901, https://doi.org/10.1088/1361-648X/aa8f79.
[40] K.F. Garrity, J.W. Bennett, K.M. Rabe, D. Vanderbilt, Pseudopotentials for high-throughput DFT calculations, Comput. Mater. Sci. 81 (2014) 446–452, https://doi.org/10.1016/j.commatsci.2013.08.053.
[41] K.B. John, P. Perdew, Matthias Ernzerhof, Generalized gradient approximation made simple, Phys. Rev. Lett. 77 (1996) 4.
[42] L.A. Agapito, S. Curtarolo, M. Buongiorno Nardelli, Reformulation of DFT+Uas a pseudohybrid hubbard density functional for accelerated materials discovery, Phys. Rev. X 5 (2015): 011006, https://doi.org/10.1103/PhysRevX.5.011006.
[43] S.H. Lee, Y.W. Son, First-principles approach with a pseudohybrid density functional for extended Hubbard interactions, Phys. Rev. Res. 2 (2020): 043410, https://doi.org/10.1103/PhysRevResearch.2.043410.
[44] K. Okhotnikov, T. Charpentier, S. Cadars, Supercell program: a combinatorial structure-generation approach for the local-level modeling of atomic substitutions and partial occupancies in crystals, J. Cheminf. 8 (2016) 17, https://doi.org/10.1186/s13321-016-0129-3.
[45] W. Setyawan, S. Curtarolo, High-throughput electronic band structure calculations: challenges and tools, Comput. Mater. Sci. 49 (2010) 299–312, https://doi.org/10.1016/j.commatsci.2010.05.010.
[46] G. Tan, F. Shi, S. Hao, H. Chi, T.P. Bailey, L.D. Zhao, C. Uher, C. Wolverton, V. P. Dravid, M.G. Kanatzidis, Valence band modification and high thermoelectric performance in SnTe heavily alloyed with MnTe, J. Am. Chem. Soc. 137 (2015) 11507–11516, https://doi.org/10.1021/jacs.5b07284.
[47] S. Chen, H. Bai, J. Li, W. Pan, X. Jiang, Z. Li, Z. Chen, Y. Yan, X. Su, J. Wu, C. Uher, X. Tang, Vacancy-based defect regulation for high thermoelectric performance in $Ge_9Sb_2Te_{12-x}$ compounds, ACS Appl. Mater. Interfaces 12 (2020) 19664–19673, https://doi.org/10.1021/acsami.0c02155.
[48] M.J. Graf, S.K. Yip, J.A. Sauls, D. Rainer, Electronic thermal conductivity and the Wiedemann-Franz law for unconventional superconductors, Phys. Rev. B Condens. Matter 53 (1996) 15147–15161, https://doi.org/10.1103/physrevb.53.15147.
[49] N. Stojanovic, D.H.S. Maithripala, J.M. Berg, M. Holtz, Thermal conductivity in metallic nanostructures at high temperature: electrons, phonons, and the Wiedemann-Franz law, Phys. Rev. B 82 (2010): 075418, https://doi.org/10.1103/PhysRevB.82.075418.
[50] Y. Liu, L.D. Zhao, Y. Liu, J. Lan, W. Xu, F. Li, B.P. Zhang, D. Berardan, N. Dragoe, Y. H. Lin, C.W. Nan, J.F. Li, H. Zhu, Remarkable enhancement in thermoelectric performance of BiCuSeO by Cu deficiencies, J. Am. Chem. Soc. 133 (2011) 20112–20115, https://doi.org/10.1021/ja2091195.
[51] L.D. Zhao, S.H. Lo, J. He, H. Li, K. Biswas, J. Androulakis, C.I. Wu, T.P. Hogan, D. Y. Chung, V.P. Dravid, M.G. Kanatzidis, High performance thermoelectrics from earth-abundant materials: enhanced figure of merit in PbS by second phase nanostructures, J. Am. Chem. Soc. 133 (2011) 20476–20487, https://doi.org/10.1021/ja208658w.
[52] L.D. Zhao, X. Zhang, H. Wu, G. Tan, Y. Pei, Y. Xiao, C. Chang, D. Wu, H. Chi, L. Zheng, S. Gong, C. Uher, J. He, M.G. Kanatzidis, Enhanced thermoelectric properties in the counter-doped SnTe system with strained endotaxial SrTe, J. Am. Chem. Soc. 138 (2016) 2366–2373, https://doi.org/10.1021/jacs.5b13276.
[53] L.X. Yuting Qiu, Xun Shi, Pengfei Qiu, Wenqing Zhang, Lidong Chen, James R. Salvador, Jung Y. Cho, Jihui Yang, Yuan-chun Chien, Sinn-wen Chen, Yinglu Tang, G. Jeffrey Snyder, Charge-compensated compound defects in Ga-containing thermoelectric skutterudites, Adv. Funct. Mater. 23 (2013) 3194–3203, https://doi.org/10.1002/adfm.201202571.
[54] C. Fu, S. Bai, Y. Liu, Y. Tang, L. Chen, X. Zhao, T. Zhu, Realizing high figure of merit in heavy-band p-type half-Heusler thermoelectric materials, Nat. Commun. 6 (2015) 8144, https://doi.org/10.1038/ncomms9144.
[55] Y. Li, T. Zhang, Y. Qin, T. Day, G. Jeffrey Snyder, X. Shi, L. Chen, Thermoelectric transport properties of diamond-like $Cu_{1-x}Fe_{1+x}S_2$ tetrahedral compounds, J. Appl. Phys. 116 (2014): 203705, https://doi.org/10.1063/1.4902849.
[56] R. Liu, L. Xi, H. Liu, X. Shi, W. Zhang, L. Chen, Ternary compound $CuInTe_2$: a promising thermoelectric material with diamond-like structure, Chem. Commun. 48 (2012) 3818–3820, https://doi.org/10.1039/c2cc30318c.
[57] Y. Cao, X. Su, F. Meng, T.P. Bailey, J. Zhao, H. Xie, J. He, C. Uher, X. Tang, Origin of the distinct thermoelectric transport properties of chalcopyrite $ABTe_2$ (A=Cu, Ag; B=Ga, in), Adv. Funct. Mater. 30 (2020): 2005861, https://doi.org/10.1002/adfm.202005861.
[58] M.L. Liu, I.W. Chen, F.Q. Huang, L.D. Chen, Improved thermoelectric properties of Cu-doped quaternary chalcogenides of $Cu_2CdSnSe_4$, Adv. Mater. 21 (2009) 3808–3812, https://doi.org/10.1002/adma.200900409.
[59] S. Pan, C. Wang, Q. Zhang, B. Yang, Y. Cao, L. Liu, Y. Jiang, L. You, K. Guo, J. Zhang, J. Yang, J. Luo, W. Zhang, $A_2Cu_3In_3Te_8$ (A = Cd, Zn, Mn, Mg): a type of thermoelectric material with complex diamond-like structure and low lattice thermal conductivities, ACS Appl. Energy Mater. 2 (2019) 8956–8965, https://doi.org/10.1021/acsaem.9b02004.
[60] S. Pan, L. Liu, Z. Li, X. Yan, C. Wang, K. Guo, J. Yang, Y. Jiang, J. Luo, W. Zhang, Embedded in-situ nanodomains from chemical composition fluctuation in thermoelectric $A_2Cu_3In_3Te_8$ (A = Zn, Cd), Materials Today Physics 17 (2021): 100333, https://doi.org/10.1016/j.mtphys.2020.100333.
[61] H. Shintani, H. Tanaka, Universal link between the boson peak and transverse phonons in glass, Nat. Mater. 7 (2008) 870–877, https://doi.org/10.1038/nmat2293.
[62] T. Brink, L. Koch, K. Albe, Structural origins of the boson peak in metals: from high-entropy alloys to metallic glasses, Phys. Rev. B 94 (2016): 224203, https://doi.org/10.1103/PhysRevB.94.224203.